Article

Interfacial Effect-Induced Electrocatalytic Activity of Spinel Cobalt Oxide in Methanol Oxidation Reaction

Salma A. Khanam, Sayanika Saikia, Seonghwan Lee, Young-Bin Park, Magdi E. A. Zaki, and Kusum K. Bania*

Read Online

ACCESS | Metrics & More | Article Recommendations | Supporting Information

ABSTRACT: In this study, spinel cobalt oxide (Co_3O_4) nanoparticles without combining with any other metal atoms have been decorated through the influence of two hard templating agents, viz., zeolite-Y and carboxy-functionalized multiwalled carbon nanotubes (COOH-MWCNT). The adornment of the Co_3O_4 nanoparticles, through the combined impact of the aluminosilicate and carbon framework has resulted in quantum interference, causing the reversal of signatory Raman peaks of Co_3O_4. Apart from the construction of small Co_3O_4 nanoparticles at the interface of the two matrices, the particles were aligned along the direction of COOH-MWCNT. The catalyst Co_3O_4-Y-MWCNT exhibited excellent catalytic activity toward the methanol oxidation reaction (MOR) in

comparison to Co_3O_4-Y, Co_3O_4-MWCNT, and bared Co_3O_4 with the current density of 0.92 A mg^{-1} at an onset potential of 1.33 V versus RHE. The material demonstrated persistent electrocatalytic activity up to 300 potential cycles and 20,000 s without substantial current density loss. High surface area of zeolite-Y in combination with the excellent conductivity of the COOH-MWCNT enhanced the electrocatalytic performance of the catalyst. The simplicity of synthesis, scale-up, and remarkable electrocatalytic activity of the catalyst Co_3O_4-Y-MWCNT provided an effective way toward the development of anode materials for direct methanol fuel cells.
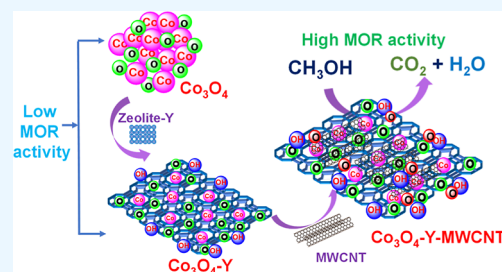
1. INTRODUCTION

The aim to mitigate the environmental damage caused by the release of greenhouse gases from petroleum and diesel engines and the target toward the zero-carbon footprint lead to the development of energy production systems that do not contribute to air and environmental pollution.[1,2] Accordingly, scientists and researchers are motivated toward the production of a H_2 fuel, design of different electrical batteries, and also biofuels.[3−6] Although a major amount of research work has been dedicated for the utilization of hydrogen (H_2) as a fuel, there are certain drawbacks that limit its commercial application.[7,8] For example, H_2 is difficult to store and transport and is also not safe due to its high inflammability. In contrast, methanol is nowadays gaining importance as it appeared to be safer, easy to transport, and more importantly, its energy density is quite good to be acceptable as a fuel.[9,10] Moreover, the byproducts that are generated from methanol fuel cells are mostly carbon dioxide (CO_2) and water (H_2O) and thus contribute very less to the environmental pollution as CO_2 can be converted into methanol (CH_3OH).[11,12]

Due to such benefits associated with CH_3OH, the researchers across the world are encouraged to develop different electrode (anode and cathode) materials for their application in direct methanol fuel cells (DMFCs).[13,14] At present, platinum (Pt)-based catalysts have been widely used in DMFCs for effective MOR. The catalysts made from Pt can easily enhance the MOR

because the range of potential [∼0.4−0.6 V vs RHE (reversible hydrogen electrode)] at which they function is substantially lesser than the predicted theoretical ORR (oxygen reduction reaction) potential functioning at 1.23 V versus RHE.[15,16] As a result, the Pt-based metal catalysts emerged as the most efficient metal catalysts that have been considered to be the best suitable catalysts for methanol oxidation reaction (MOR) in DMFCs. However, Pt suffers from few limitations, like its high cost, more importantly, the carbon monoxide (CO) poisoning that retards the Pt activity during MOR that leads the researchers to mostly focus on non-Pt-based metal catalysts.[17,18] The non-Pt-based catalysts are not only cost-effective but also less susceptible to CO poisoning. However, one of the major challenges in non-Pt based metal catalysts is to overcome the kinetic retardness and to perform the MOR at low onset potential with good current density to compete with Pt-based catalysts. With the growing interest for sustainable development, from our group, we have reported some of the non-platinum (Pt)-derived electrocatalysts that served as a suitable anodic material that displayed high

current density with a reasonable onset potential in the electrochemical oxidation of methanol.[19−21] Apart from the preparation of the non-noble-metal-based catalyst, emphasis has been given to the synthesis of catalysts that can be sustained in alkaline media. Literature findings insisted that the MOR process is more feasible in basic media in comparison to that of acidic electrolytes.[22,23] It has been found that the MOR process in an alkaline electrolyte resulted in low poisoning of the catalyst, and it also improves the stability and efficiency and thereby favor the recyclability of the catalyst.[24,25] During our continuous endeavor, we have encountered that the zeolite-Y and carboxy-functionalized multiwalled carbon nanotube (COOH-MWCNT) provides a suitable environment for the decoration of fine nanoparticles by acting themselves as solid support and as well as hard template.[26,27] The zeolite-Y with its surface hydroxyl (−OH) group renders a high metal to surface interaction and controls the growth of nanoparticles without being agglomerated. While the COOH-MWCNT provides a good conducting media to improve its current efficiency.[19,28]

In the recent years, apart from our group, many other researchers have also used zeolites as supports for the decoration of the electrocatalyst for MOR.[29−31] In this regard, the cobalt oxide is finding importance due to its good redox activity. They have been widely used as an effective catalyst in the water oxidation reaction and in the current scenario; cobalt oxide has been combined with different metals like Cu, Ni, Sn, W, Rh, etc. for application in MOR.[32−38] However, the cobalt oxide catalyst entrapped at the interface of zeolite Y and carboxy-functionalized MWCNT has not been reported elsewhere. Zeolites due to its porosity as well as the carbon nanotubes with their cylindrical channels can modify the electronic environment of metal oxides.[30,39] Therefore, to understand such an impact on the activity of spinel cobalt oxide (Co_3O_4), herein, we tried to decorate Co_3O_4 at the surface interface of two hard templating agents and to see its activity in the MOR process.

2. EXPERIMENTAL SECTION

2.1. Materials. Cobalt(II) chloride hexahydrate ($CoCl_2 \cdot 6H_2O$) was obtained from E. Merck and utilized as a source of cobalt. Sigma-Aldrich provided the Nafion solution, zeolite-Y, and multiwalled carbon nanotubes (COOH-MWCNT). From E. Mark, sodium hydroxide (NaOH), potassium hydroxide (KOH), and ethanol (C_2H_5OH) were obtained. The 1 M KOH solution was made with deionized water. E. Merck provided dried methanol (CH_3OH) for the MOR.

**2.2. Synthesis of Co_3O_4.** Co_3O_4 has been synthesized by using $CoCl_2 \cdot 6H_2O$ as precursor material by the precipitation method. In a round-bottom flask, a solution of 1 M NaOH and 0.1 M $CoCl_2 \cdot 6H_2O$ was mixed and stirred for about 1 h. The precipitate obtained was filtered and then washed with distilled water (H_2O) for the removal of the unreacted materials. The material was then dried in a hot air oven at 333 K and dried under vacuum at 343 K. After that, the material obtained was calcined at 673 K for about 3 h by means of a muffle furnace. The resulting material was Co_3O_4.

2.3. Synthesis of Zeolite-Y-Supported Cobalt Oxide, Co_3O_4-Y Electrocatalyst. The zeolite-Y supported catalyst Co_3O_4-Y was synthesized by using the previously reported procedure by our group with a slight modification. In a round-bottom flask, $Co(OH)_2$ was precipitated over zeolite Y using 0.1 M (50 mL) $CoCl_2 \cdot 6H_2O$ solution in the presence of 0.1 M NaOH solution to develop cobalt (Co) electrocatalysts supported by zeolite-Y. At 373 K, the solution was refluxed for

about 24 h. In order to eliminate the unreacted materials, the precipitate that had formed was first filtered under pressure and repeatedly washed away with water. After that, the material was dried out in a hot air oven at 348 K and dried under vacuum for about 6 h at 353 K. After that, the compound was calcined at 673 K in a muffle furnace. The blackish-gray colored powdered material, Co_3O_4-Y, was obtained after grinding the calcined material for about 5 h in a mortar and pestle with the addition of ethanol drop by drop.

2.4. Modification of an Co_3O_4-Y Electrocatalyst with COOH-MWCNT (Co_3O_4-Y-MWCNT). A portion of Co_3O_4-Y (1 g) was taken with 0.05 g of COOH-MWCNT in a mortar. After that, it was ground for 2−3 h. While grinding, a small amount of (C_2H_5OH) solution was added to the above mixture dropwise. It was then heated for a specific period at 393 K. The solid material was produced after nearly 50−60 h of subsequent heating and grinding. The process of synthesis of Co_3O_4-Y-MWCNT has been demonstrated in Scheme 1.

Scheme 1. Synthesis of Zeolite-Y-Supported Co_3O_4 Electrocatalyst Modified with COOH-MWCNT
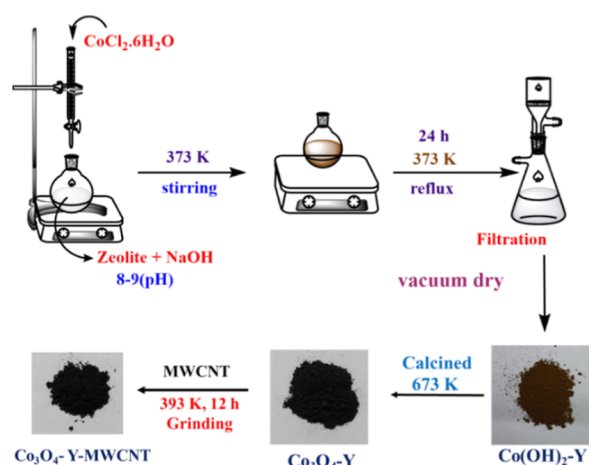
2.5. Physical Measurements. The Supporting Information contains information about the physical measurements performed in this study.

2.6. Electrochemical Measurements. The electrochemical activity of the materials was examined using a three-electrode system wherein a glassy carbon electrode (GCE) was utilized as the working electrode, a standard calomel electrode (SCE) was used as the reference electrode, and a graphite rod was utilized as the counter electrode. Before the modification, the GCE was properly cleaned using alumina slurry and then for about 30 min, electrodes were ultrasonicated in ethanol (C_2H_5OH) and deionized water (H_2O). An aliquot was made by dissolving 1 mg of each active catalyst in 1 mL of C_2H_5OH/H_2O with 20 μL (0.5% w/w) of Nafion solution. For 60 min, the mixture was constantly sonicated in order to generate the homogeneous ink. Drop casting of 20 μL homogeneous materials over a glassy carbon electrode that was cleaned previously generated the working electrode. The as-prepared GCE was dried properly in a N_2 atmosphere. The electrochemical properties of the synthesized materials were done by using cyclic voltammetry (CV), linear sweep voltammetry (LSV), chronoamperometry (CA), and electrochemical impedance spectroscopy (EIS) measurements in an alkaline medium using 1 M KOH solution. In all electrochemical tests,
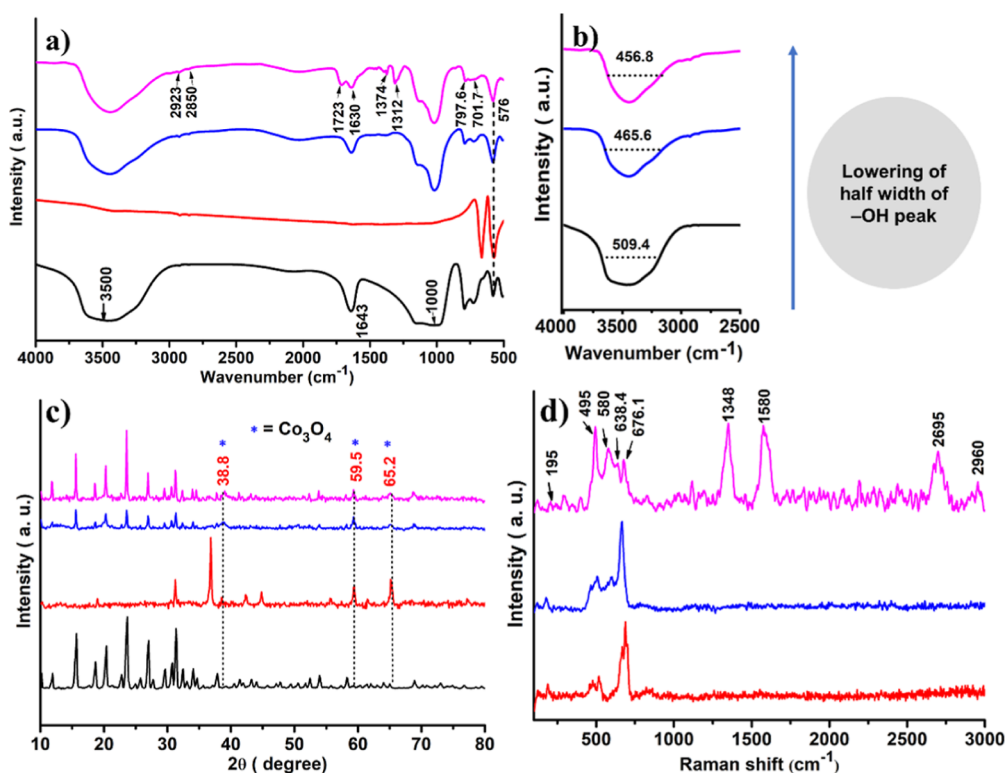
Figure 1. (a) IR spectrum of neat zeolite-Y (black), Co_3O_4 (red), Co_3O_4-Y (blue), and Co_3O_4-Y-MWCNT (pink) and (b) half width measurement plot of the −OH peak of neat zeolite-Y (black), Co_3O_4-Y (blue), and Co_3O_4-Y-MWCNT (pink). (c) PXRD pattern of neat zeolite (black), Co_3O_4 (red), Co_3O_4-Y (blue), and Co_3O_4-Y-MWCNT (pink), respectively. (d) Raman spectra of Co_3O_4 (red), Co_3O_4-Y (blue), and Co_3O_4-Y-MWCNT (pink).

the current density was determined with regard to the total loaded mass of catalysts Co_3O_4-Y and Co_3O_4-Y-MWCNT as 0.110 and 0.125 mg cm^{-2}. The electrochemical measurements were performed with *iR* correction built in to the instrument. Potentials were measured with regard to SCE (standard calomel electrode), E_{SCE}, and reported versus RHE (reversible hydrogen electrode), E_{RHE}, in this work. The following relation was used to convert E_{SCE} into E_{RHE}.

$$E_{RHE} = E_{SCE} - E^\circ_{H_2/H^+} + 0.244 \qquad (1)$$

where $E^\circ_{H_2/H^+}$ represents the reversible hydrogen potential ($E^\circ_{H_2/H^+} = -0.059$ pH), given by the Nernst equation. The pH value of the test solution (1 M KOH) was measured to be ∼14. The number +0.244 in eq 1 signifies the standard potential (in volts) of the used SCE at 25 °C.

3. RESULTS AND DISCUSSION

The characterization of the synthesized materials was done by means of various analytical techniques. The synthesized materials, Co_3O_4, Co_3O_4-Y, and Co_3O_4-Y-MWCNT were first characterized by using Fourier transform infrared (FTIR) analysis. The FTIR spectra of neat zeolite-Y, Co_3O_4, Co_3O_4-Y, and Co_3O_4-Y-MWCNT are shown in Figure 1a. For the neat zeolite-Y, the sharp band observed at ∼1000−1100 cm^{-1} is accredited to the asymmetric vibration (stretching) of the (Si/Al)O_4 units, Figure 1a (black). The IR peak at ∼1643 cm^{-1} resembles to the −OH bending vibration and ν_{as} (Si−OH of zeolite-Y) appeared at ∼3500 cm^{-1}.[40] The IR spectrum of unsupported Co_3O_4 [Figure 1a (red)] exhibited two peaks at 565 and 660 cm^{-1} for the Co−O bond in Co_3O_4. The IR peak at

660 cm^{-1} signified the Co^{3+}−O (octahedral site) vibration, and the peak at 555 cm^{-1} was assigned to the Co^{2+}−O (tetrahedral site) vibration originated from Co_3O_4.[41,42] The IR spectrum of zeolite-Y supported Co_3O_4, i.e., Co_3O_4-Y has been shown in Figure 1a (blue). Due to the lower concentration of metal oxide the zeolite-Y supported catalyst; Co_3O_4-Y had not shown any specific distinguishable peak in the spectrum. However, a slight change of intensity and broadness of the peaks occurred in the region 400−800 cm^{-1} which indicated the formation of a metal oxide.[41] The IR spectrum of the COOH-MWCNT modified catalyst Co_3O_4-Y-MWCNT is shown in Figure 1a (pink). The peak detected at ∼1723 cm^{-1} matches to the C=O bond stretching vibration of the carboxyl (−COOH) group of COOH-MWCNT. The IR peak observed at 1312 and 1374 cm^{-1} corresponds to the C−O stretching of the −COOH group of COOH-MWCNT. The band observed at 1630 cm^{-1} was attributed to the C=C vibration of aromatic rings of COOH-MWCNT.[43] The slight IR band observed at ∼2923 and 2850 cm^{-1} accredited to methylene's C−H stretching vibration created at the defect site of the COOH-MWCNT surface.[44] Figure 1b shows the half width measurement plot of the −OH peak of zeolite-Y (black), Co_3O_4-Y (blue), and Co_3O_4-Y-MWCNT (pink). From the half width measurement of the −OH peak, it was observed that the peak half width got reduced on modifying the zeolite-Y with Co_3O_4 and further modifying with COOH-MWCNT. The decrease in peak width from 509.4 cm^{-1} in zeolite-Y to 456.8 cm^{-1} in Co_3O_4-Y-MWCNT implied that the carboxylate group (−COOH) of the COOH-MWCNT interacted with zeolite-Y's surface −OH group and with the Co_3O_4 surface. The catalysts Co_3O_4, Co_3O_4-Y, and Co_3O_4-Y-MWCNT were further characterized by powder X-ray
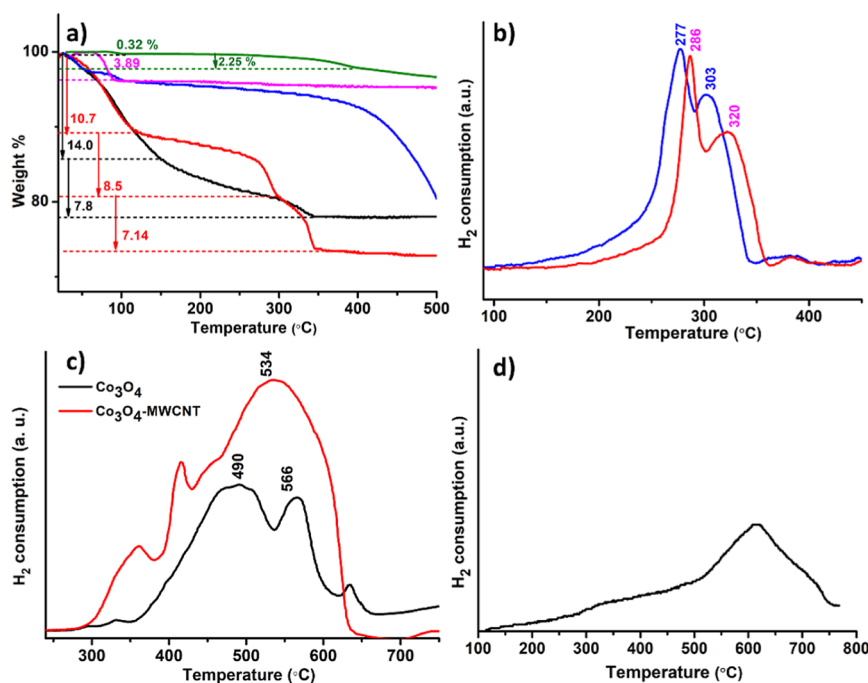
Figure 2. (a) TGA plot of Co_3O_4 (pink), COOH-MWCNT (blue), Co_3O_4-MWCNT (green), Co_3O_4-Y (black), and Co_3O_4-Y-MWCNT (red). H_2-TPR profile of (b) Co_3O_4-Y (blue) and Co_3O_4-Y-MWCNT (red), (c) Co_3O_4 (black) and Co_3O_4-MWCNT (red), and (d) COOH-MWCNT.

diffraction (PXRD) study. The PXRD plots of all of the materials are depicted in Figure 1c. The PXRD plot of neat zeolite-Y is shown in Figure 1c (black). The PXRD plot of Co_3O_4 is shown in Figure 1c (red). It shows diffraction peaks (in degrees) at 19.1, 31.3, 36.8, 38.8, 44.8, 59.5, and 65.2 corresponding to (1 1 1), (2 2 0), (3 1 1), (2 2 2), (4 0 0), (5 1 1), and (4 4 0) planes of spinel Co_3O_4, respectively.[45] Co_3O_4-Y catalysts depicted in Figure 1c (blue) showed the peak at 38.8, 59.5, and 65.2° corresponding to (2 2 2), (5 1 1), and (4 4 0) planes of spinel Co_3O_4, respectively.[46] The PXRD plot of MWCNT-modified Co_3O_4-Y, i.e., Co_3O_4-Y-MWCNT, is shown in Figure 1c (pink). The material exhibited PXRD peaks at 38.8, 59.5, and 65.2° corresponding to (2 2 2), (5 1 1), and (4 4 0) planes of spinel Co_3O_4.

The Raman spectrum of the synthesized catalyst Co_3O_4 (red), Co_3O_4-Y(blue), and Co_3O_4-Y-MWCNT (pink) are shown in Figure 1d. Co_3O_4 is expected to show five Raman active modes $(1A_{1g} + 1E_g + 3F_{2g})$ according to the group theory.[47] For Co_3O_4-Y, five Raman bands were observed at ~180, 470, 508, 606, and 668 cm^{-1}, Figure 1d (blue). The Raman peak at ~180 cm^{-1} resembled F_{2g} (1) symmetry. This peak corresponds to the tetrahedral site of the Co_3O_4 spinel structure. The peak observed at 470 cm^{-1} has been arisen from E_{2g} symmetry, while the Raman peak located at 508 and 606 cm^{-1} originated from the F_{2g} (2) symmetry and F_{2g} (3) symmetry, respectively. The sharp peak at 668 cm^{-1} (A_{1g} symmetry) referred to the CoO_6 (octahedral sites) of the Co_3O_4 phase.[48] After modification with COOH-MWCNT, the Raman peaks were observed with a slight shift to ~190, 495, 580, 638, and 676 cm^{-1} with the reversal of the peak intensities, Figure 1d (pink). Such reversal in Raman signal after the modification of Co_3O_4 with COOH-MWCNT was attributed to quantum interference that is sometimes observed in two-dimensional layered materials.[49] However, such an effect of quantum interference has not been so far observed in the case of spinel Co_3O_4. There are of course few reports on such Raman scattering with the reversal of peak

intensities, e.g., Zhang et al. reported quantum interference-induced chiral Raman scattering in monolayers ReS_2 and $ReSe_2$.[49,50] Osiekowicz et al. observed a strong variation in the intensity of phonon modes due to the resonance condition of Raman scattering in γ-InSe and ε-GaSe crystals that was described in terms of quantum interference as well as electron−phonon coupling.[51] Chen et al. revealed the role of quantum interference in Raman scattering between distinct paths in graphene.[52] Co_3O_4-Y-MWCNT additionally showed two sharp peaks resembling to the D (disorder) and G (graphite) bands at 1348 and 1580 cm^{-1}, respectively. Another distinct peak at ~2695 cm^{-1} was detected for the second order overtone (2D) of the D band. The slight Raman peak that seemed at ~2960 cm^{-1} corresponds to the D + G band of the COOH-MWCNT.[53] This implied the encapsulation of Co_3O_4 nanoparticles over zeolite-Y and COOH-MWCNT.

For practical application of anode materials in DMFCs, the thermal stability of the catalyst as well as the reduction property of the metal with respect to temperature change plays an important role.[54] Therefore, to understand the thermal stability and the reduction temperature of Co_3O_4 before and after modification, the thermogravimetric analysis (TGA) and temperature-programmed reduction (TPR) analysis were performed.[55] TGA plot of Co_3O_4 (pink), COOH-MWCNT (blue), Co_3O_4-MWCNT (green), Co_3O_4-Y (black), and Co_3O_4-Y-MWCNT (red) are shown in Figure 2a. In the case of bare Co_3O_4 (pink), 3.89% weight loss was observed in the temperature range of 68 to 102 °C resulting from the elimination of absorbed H_2O molecules. In the case of COOH-MWCNT, a small mass loss was detected in the temperature range of 0−400 °C, and after that, the material started to decompose, Figure 2a (blue).[56,57] In the case of Co_3O_4-MWCNT, 0.32 and 2.25% weight losses were observed up to ~105 and ~400 °C, respectively, implying that the thermal stability of Co_3O_4 was improved on modification with MWCNT. For the material Co_3O_4-Y, a weight loss of 14.0%
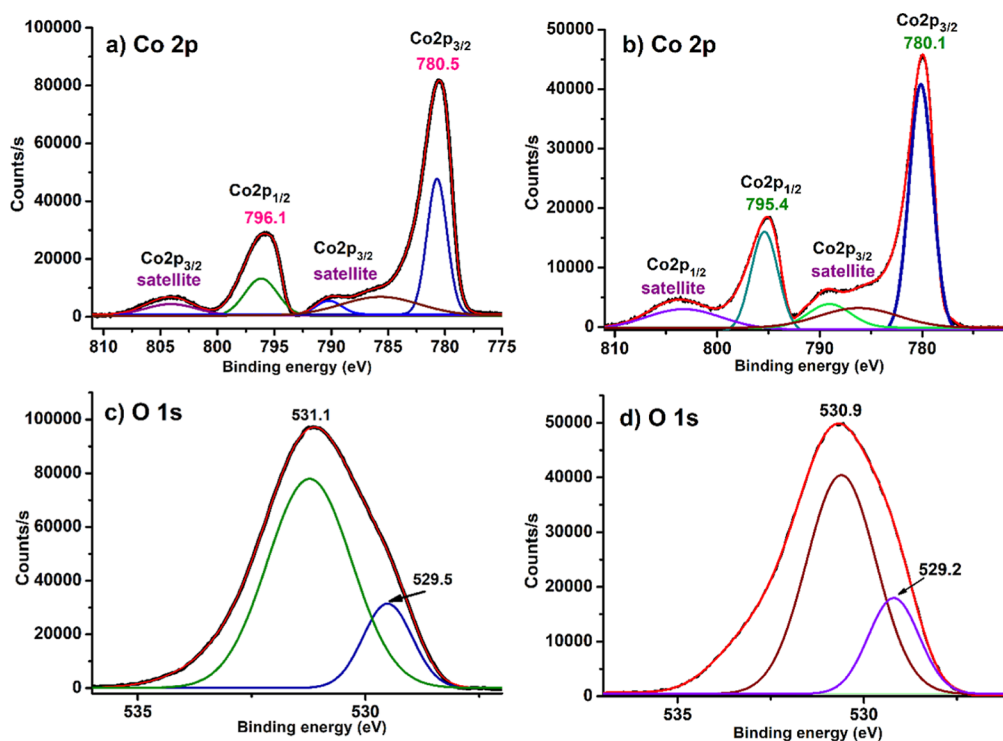
Figure 3. Co 2p XPS were recorded in (a) Co_3O_4-Y and (b) Co_3O_4-Y-MWCNT. O 1s XPS spectra in (c) Co_3O_4-Y and (d) Co_3O_4-Y-MWCNT.

was observed in the range of ~35 to 145 °C due to the elimination of absorbed water molecules. The weight loss of 7.8% in the temperature range of ~145 to 345 °C was observed due to elimination of the surface hydroxyl (−OH) group, Figure 2a (black). In the case of Co_3O_4-Y-MWCNT, weight losses of 10.7% up to ~120 °C and 8.5% up to 297 °C were observed resulting from the loss of water molecules absorbed on the surface and evaporation of interlayered water molecules. A weight loss of 7.14% was occurred in the ~297 to 345 °C temperature range due to the functional group decomposition, Figure 2a (red).[58−60] From TGA, it was evident that the thermal stability was highly influenced on hybridizing with zeolite-Y which suggested that the Co_3O_4 nanoparticles interacted more strongly with the surface −OH group of zeolite-Y leading to the weakening of bond strength of supported materials (zeolite-Y and MWCNT).

Temperature-programmed profiles of the materials are presented in Figure 2b−d. Co_3O_4-Y showed two reduction peaks accredited to the reduction of Co^{3+} to Co^{2+} at 277 °C and Co^{2+} to metallic Co at 303 °C, as shown in Figure 2b (blue).[61] In the case of Co_3O_4-Y-MWCNT, the reduction peak shifted to 286 and 320 °C, respectively, as depicted in Figure 2b (red). This specified the higher stability of the Co_3O_4-Y-MWCNT catalyst in comparison to the Co_3O_4-Y. The TPR data of Co_3O_4-Y-MWCNT was also compared with bare Co_3O_4, Figure 2c (black). It was interesting to observed that the reduction temperature of the bare Co_3O_4 appeared significantly at a higher temperature region (at 490 °C for Co_3O_4 to CoO and at 566 °C for CoO to Co). Similarly, in the case of Co_3O_4-MWCNT [Figure 2c (red line)], CoO to Co reduction was found at 534 °C, slightly lower than that of the bared Co_3O_4. The TPR profile of COOH-MWCNT is shown in Figure 2d and was observed to be completely different from the catalysts showing a low intense reduction peak above 600 °C.

The change in the reduction temperature was attributed to the difference in the crystallite size of Co_3O_4 in the bare and supported ones. Similar difference in reduction temperature of Co_3O_4 with respect to the change in crystallite size was also observed by Li et al. and James and Maity.[62,63] The comparison of the TPR profile implied that the Co_3O_4 species in the hybrid catalyst was reducible at a low temperature. This implied that zeolite-Y played a dominant role in controlling the crystallite size of Co_3O_4 and provided information that reduction of Co(III) to Co(0) can be achieved at a lower temperature by tuning the crystallite size of the metal oxide, which may further help in designing of a newer material for the methanol oxidation reaction. This TPR analysis was found to be in accordance with TGA. The UV−visible diffuse reflectance spectra (DRS) of the catalysts Co_3O_4-Y and Co_3O_4-Y-MWCNT are shown in Figure S1 of the Supporting Information. The DRS spectra of both materials demonstrated high absorption ability, particularly in the absorption range of 200−800 nm. The transition of charge from the oxygen (O) to cobalt (Co) orbital was indicated by the resulting two broad peaks in this region. In the case of both catalysts, three adsorption peaks were obtained in the range of 250−280 nm ($O^{2−}$ of zeolite to Co metal), 385−415 nm ($O^{2−}$ to Co^{2+} charge transfer transition), and 690−740 nm ($O^{2−}$ to Co^{3+} charge transfer transition), indicating double oxidation state of the synthesized materials.[64,65] The oxidation state of the synthesized catalyst Co_3O_4-Y and Co_3O_4-Y-MWCNT was established by X-ray photoelectron spectroscopy (XPS) analysis. The Co 2p spectrum of Co_3O_4-Y and Co_3O_4-Y-MWCNT has been depicted in Figure 3a,b. The spectra showed signals at a binding energies of 780.5 ± 0.4 eV for Co $2p_{3/2}$ and at 796.1 ± 0.3 eV for Co $2p_{1/2}$. The weak satellite structure appeared at 790.1 ± 0.2 and 804.5 ± 0.4 eV for the XPS spectrum of Co $2p_{3/2}$ and Co $2p_{1/2}$, respectively, provided a strong evidence for the formation of the Co_3O_4 spinel structure.[19] The O 1s XPS spectrum of Co_3O_4-Y and Co_3O_4-

Y-MWCNT are depicted in Figure 3c,d. The peaks observed at 529.5 and 529.2 eV for O 1s of Co_3O_4-Y and Co_3O_4-Y-MWCNT, respectively, confirmed the formation of metal oxide, i.e., Co_3O_4.[66] The peak at 531.1 ± 0.2 eV was observed due to the presence of Al_2O_3 (alumina) in both the materials.[67] The XPS spectrum of aluminum (Al) and silicon (Si) are depicted in Figure S2 of the Supporting Information. For the material Co_3O_4-Y as illustrated in Figure S2a, the binding energy value for Al $2p_{1/2}$ was found at 74.0 eV and for Co_3O_4-Y-MWCNT as shown in Figure S2b, it was observed at 73.6 eV. The XPS spectrum of Si 2p (Figure S2) showed the signal for SiO_4^{4-} at 102.5 and 102.3 eV for Co_3O_4-Y (Figure S2c) and Co_3O_4-Y-MWCNT (Figure S2d), respectively.[68,69] As shown in Figure S3, four signals were observed at ~284.3, 284.8, 286.1, and 288.6 eV which attributes to the C=C (sp^2), C=C (sp^3), C−OH, and O=C−OH species present in the C 1s XPS spectrum of Co_3O_4-Y-MWCNT.[40,70]

Scanning electron microscopy (SEM) and transmission electron microscopy (TEM) analyses were done to observe the morphological characteristics of the catalyst Co_3O_4-Y-MWCNT. The SEM images of the prepared catalyst Co_3O_4-Y-MWCNT are shown in Figure 4a,b. The images indicated that the zeolite Y incorporated Co_3O_4 was engulfed with MWCNT.
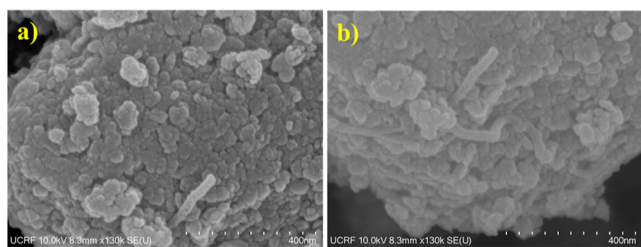

Figure 4. (a,b) SEM images of Co_3O_4-Y-MWCNT.

The TEM images of the catalyst Co_3O_4-Y-MWCNT are shown in Figure 5a−e. TEM images depict the formation of Co_3O_4 nanoparticles at the zeolite-Y and COOH-MWCNT interfaces. Most interestingly, it was observed that the nanoparticles were decked along the direction of the nanotubes,

as shown in Figure 5d, marked by yellow lines. This further implied that COOH-MWCNT not only served as a surface matrix but also acted as a shape directing hard templating agent. The same was also observed from the TEM image of the catalyst Co_3O_4-Y-MWCNT, Figure 5e. The lattice fringe pattern of ~0.24 and 0.46 nm as shown in Figure 5f signified the (3 1 1) and (1 1 1) lattice planes of Co_3O_4, respectively.[71] This implied the presence of Co_3O_4 at the zeolite-Y and the COOH-MWCNT surface interface.

The scanning transmission electron microscopy energy dispersive X-ray (STEM-EDX) elemental mapping analysis revealed the existence of elements cobalt (Co), oxygen (O), aluminum (Al), silicon (Si), and carbon (C) in the as-prepared catalyst, Co_3O_4-Y-MWCNT. The images of STEM-EDX mapping for the material Co_3O_4-Y-MWCNT are shown in Figure 6a−f. The corresponding EDX spectra of the catalyst Co_3O_4-Y-MWCNT are shown in Figure 6g. From EDX mapping, the weight % of Co, O, Al, Si, and C were found to be 52.21, 29.03, 4.43, 9.41, and 4.49%, respectively. The atomic % of Co, O, Al, Si, and C were obtained to be 26.93, 54.53, 4.92, 10.03, and 3.59%, respectively, Figure 6h. The STEM-EDX mapping images of Co_3O_4-Y-MWCNT in a different region has also been provided in the Figure S4. Those EDX mapping images also provided evidence of the growth of Co_3O_4 in the direction of nanotubes and surrounding the zeolite crystals.

4. ASSESSING ELECTROCATALYTIC ACTIVITY OF THE SYNTHESIZED CATALYST IN MOR

The MOR activity of the synthesized materials Co_3O_4, Co_3O_4-Y, and Co_3O_4-Y-MWCNT were evaluated by performing the cyclic voltammetry (CV) analysis between −1.0 and 1.4 V scan rate (Ag/AgCl) to obtain the best catalyst for MOR. First, the CV experiment was performed with catalysts modified the GC electrode in the absence of CH_3OH with 1 M KOH at 50 mV s^{-1} scan rate. The catalysts Co_3O_4-Y and Co_3O_4-Y-MWCNT exhibited a minor oxidation peak during the forward scan at onset potentials of 1.45 and 1.41 V versus RHE, respectively. However, it did not exhibit any significant signal for the OER. The CV plots for Co_3O_4-Y and Co_3O_4-Y-MWCNT in 1 M KOH are shown in Figures S5 and S6. After that, the CV experiment
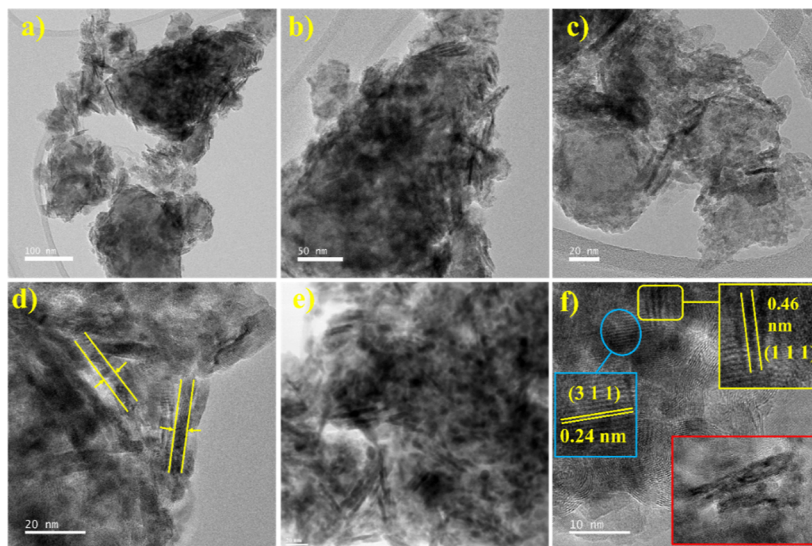

Figure 5. Morphological illustration of Co_3O_4-Y-MWCNT. (a−e) TEM images of Co_3O_4-Y-MWCNT at different resolutions. (f) High-resolution TEM image showing the fringe pattern of Co_3O_4-Y-MWCNT corresponding to spinel Co_3O_4.
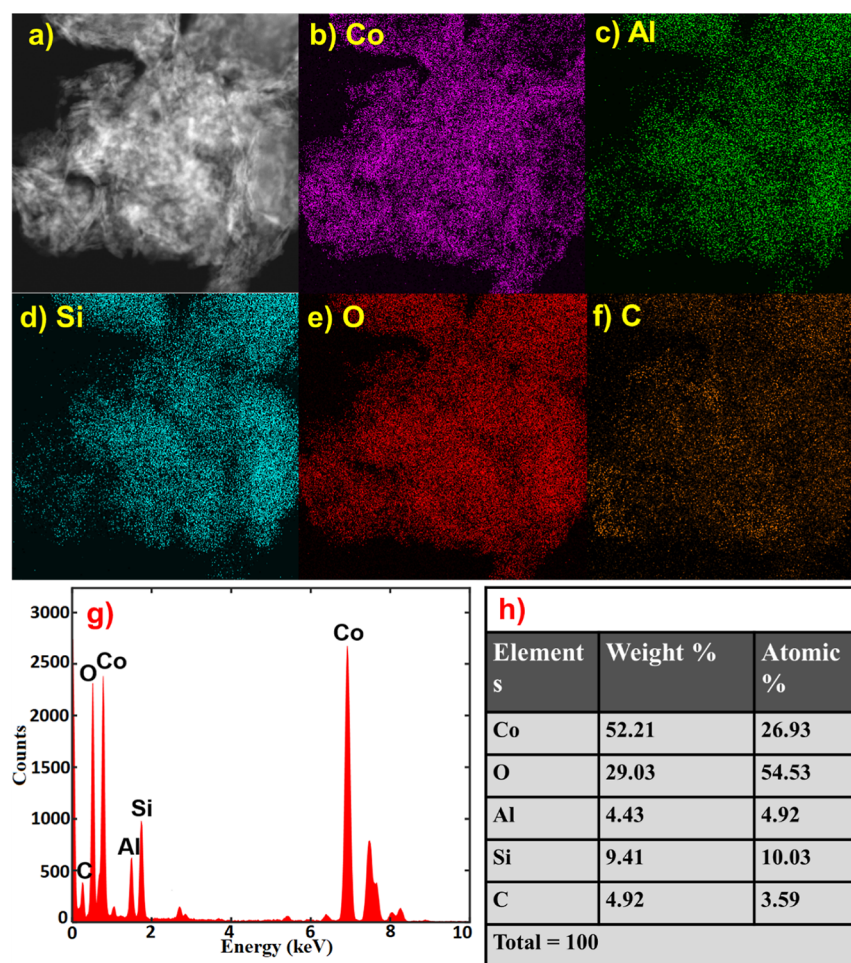
Figure 6. (a) HAADF-STEM (high-angle annular dark-field scanning transmission electron microscopy) electron image utilized for the EDX analysis of Co_3O_4-Y-MWCNT. EDX mapping image of (b) Co, (c) Al, (d) Si, (e) O, and (f) C. (g) Corresponding EDX spectra, (h) percentage weight, and atomic percentage of the corresponding elements.

was done at a scan rate of 50 mV s^{-1} by the addition of a 1 M CH_3OH solution to the 1 M KOH solution, Figure 7a. It is pertinent to mention herein that the COOH-MWCNT support although conducting in nature did not show any MOR activity as observed from the CV curve shown in Figure 7a (black). In the case of a bare Co_3O_4 catalyst, the CH_3OH oxidation took place with a current density of 0.33 A mg^{-1} at an onset potential of 1.45 V versus RHE, Figure 7a (red). In the case of Co_3O_4-MWCNT, the current density was measured to be 0.72 A mg^{-1}. Although the current density was found to increase, the onset potential was found to be 1.45 V versus RHE, Figure 7a (blue). The zeolite-Y modified Co_3O_4 showed better MOR activity than the bare Co_3O_4 catalyst at 1.33 V versus RHE onset potential with a current density of 0.78 A mg^{-1}, Figure 7a (pink). The catalyst Co_3O_4-Y-MWCNT showed sharp a oxidation peak with the highest peak current density of 0.92 A mg^{-1} at an onset potential 1.33 V versus RHE [Figure 7a (green)] implying the sufficient ability of the catalyst toward MOR. From this analysis, it was evident that Co_3O_4 was the active species for MOR, while the MWCNT and zeolite-Y served as the solid support as well as the hard templating agent for the controlled growth of the Co_3O_4 nanocatalyst, providing a good surface to metal interaction through their surface functional groups like −OH in zeolite-Y and −COOH in COOH-MWCNT. Because of such an impact from these two surfaces, the activity of bared Co_3O_4 toward MOR was improved in terms of onset potential as well as

the current density. It was further evident from Figure 7a that MWCNT alone cannot oxidize the CH_3OH but the combination of MWCNT with Co_3O_4 or Co_3O_4-Y improved the MOR activity by providing a conducting surface and thereby enhancing the current density. Since the COOH-MWCNT modified catalysts Co_3O_4-Y-MWCNT showed the highest activity for MOR, the other electrochemical measurements were done by using Co_3O_4-Y-MWCNT as an anode catalyst. The CV of scan rate variation, concentration variation, multicycle stability test, and chronoamperometry (CA) test and linear sweep voltammetry (LSV) for the Co_3O_4-Y-MWCNT catalyst were performed and are illustrated in Figure 7. The scan rate variation, LSV, multicycle stability test, and CA experiments were accomplished in 1 M KOH and 1 M MeOH solution maintaining pH 14. Figure 7b presents the CV curves of Co_3O_4-Y-MWCNT by varying the scan rate from 10 to 100 mV s^{-1}. With the increase in scan rate, the current density gradually increased to higher value and the anodic (oxidation) peak position switched to a higher potential. The peak current density was related proportionally to the square root of the scan rate from 10 to 100 mV s^{-1} with a value of R^2 = 0.98, indicating a diffusion-limited reaction.[72] The LSV plot of scan rate variation showing the onset potential (1.33 V vs RHE) has been depicted in Figure 7c. To examine the CH_3OH concentration tolerance of the catalysts, the CV experiment were performed by varying the CH_3OH concentration. The current density of MOR was shown
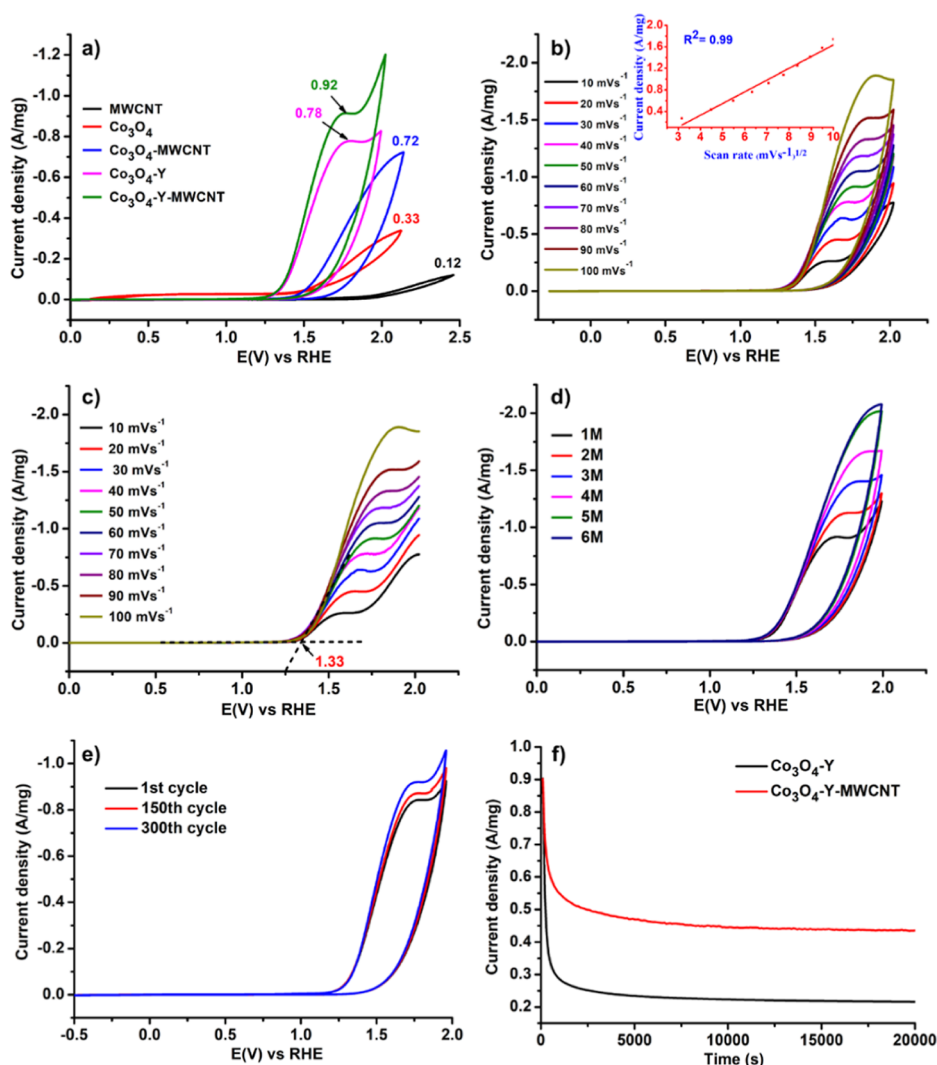
Figure 7. Electrochemical MOR performance of synthesized materials. (a) CV curves of MOR at 50 mV s^{-1} in 1 M KOH for COOH-MWCNT (black), Co$_3$O$_4$ (red), Co$_3$O$_4$-MWCNT (blue), Co$_3$O$_4$-Y (pink), and Co$_3$O$_4$-Y-MWCNT (green) with 1 M CH$_3$OH. CVs of (b) scan rate variation and (c) LSV plot showing the onset potential = 1.33 V vs RHE with 1 M KOH and 1 M CH$_3$OH at a scan rate 10−100 mV s^{-1} for Co$_3$O$_4$-Y-MWCNT. (d) CV at a scan rate of 50 mV s^{-1} showing concentration change of CH$_3$OH from 1 to 6 M with 1 M KOH. (e) CV depicting a multicycle stability test for Co$_3$O$_4$-Y-MWCNT with 1 M KOH and 1 M CH$_3$OH (50 mV s^{-1} scan rate). (f) CA response of the Co$_3$O$_4$-Y-MWCNT electrode in 1 M KOH and 1 M CH$_3$OH at 0.5 V for 20,000 s.

to be directly proportional to the concentration of CH$_3$OH up to a particular point, after which the regular increase in current density was no more observed with the increase in CH$_3$OH concentration. With the rise in CH$_3$OH concentration, the current density increases slightly and become stabilized at 6 M, as depicted in Figure 7d. The Co$_3$O$_4$-Y-MWCNT electrode displayed current densities of 1.12 A mg^{-1} at 2 M, 1.41 A mg^{-1} at 3 M, 1.66 A mg^{-1} at 4 M, 2.01 A mg^{-1} at 5 M, and 2.07 Am g^{-1} at 6 M CH$_3$OH concentration. This peculiar behavior of the current density enhancement can be explained by the accompanying change in rate control stage of the method of catalysis. When the concentration of CH$_3$OH was low in the MOR process, the rate control step was conquered by reactive species diffusion, demonstrating a continuous increase in the current density up to 5 M CH$_3$OH. An additional increase in the concentration of CH$_3$OH resulted in a mixed-control procedure that is dependent on both catalytic and diffusion kinetics. This effect resulted in a slight increase in the current density of MOR with increasing CH$_3$OH concentration. Furthermore, beyond a

specific CH$_3$OH concentration limit, the CH$_3$OH oxidation on the surface of the electrode became a reaction-kinetics regulated process. Following that, the current density became saturated and is controlled by the electrocatalytic behavior of the electrode. The ability of an anode material to hold its stability without much loss of current density for abundant potential cycles is one of the most important parameters for its practical applicability in DMFCs. The stability of the Co$_3$O$_4$-Y-MWCNT modified electrode was examined by conducting a multicycle stability test at the scan rate of 50 mV s^{-1}. Continuous scanning for three hundred (300) cycles were done and the result was evaluated. As shown in Figure 7e, the electrode lost 6.4% (150th cycles) and 8.6% (300th cycles) of the current density of the first cycle of CV at 1.33 V onset potential. CA test was also executed to see the enduring constancy of the Co$_3$O$_4$-Y-MWCNT-based electrode at 0.5 V for 20,000 s, as shown in Figure 7f. An improved performance of CA was obtained for the Co$_3$O$_4$-Y-MWCNT catalyst in comparison to Co$_3$O$_4$-Y.
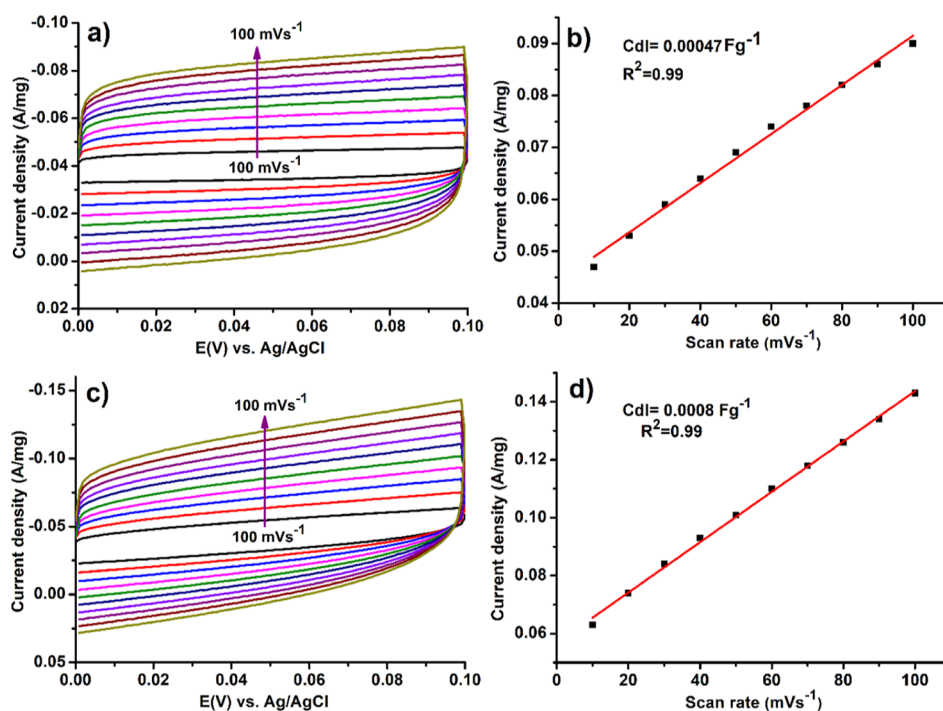
Figure 8. (a) CVs at a non-Faradaic region (0−0.1 V vs Ag/AgCl) with 1 M KOH (10−100 mV s^{-1} scan rate), (b) CV curve of current density vs scan rate for Co$_3$O$_4$-Y, and (c,d) equivalent CV and plot for Co$_3$O$_4$-Y-MWCNT.
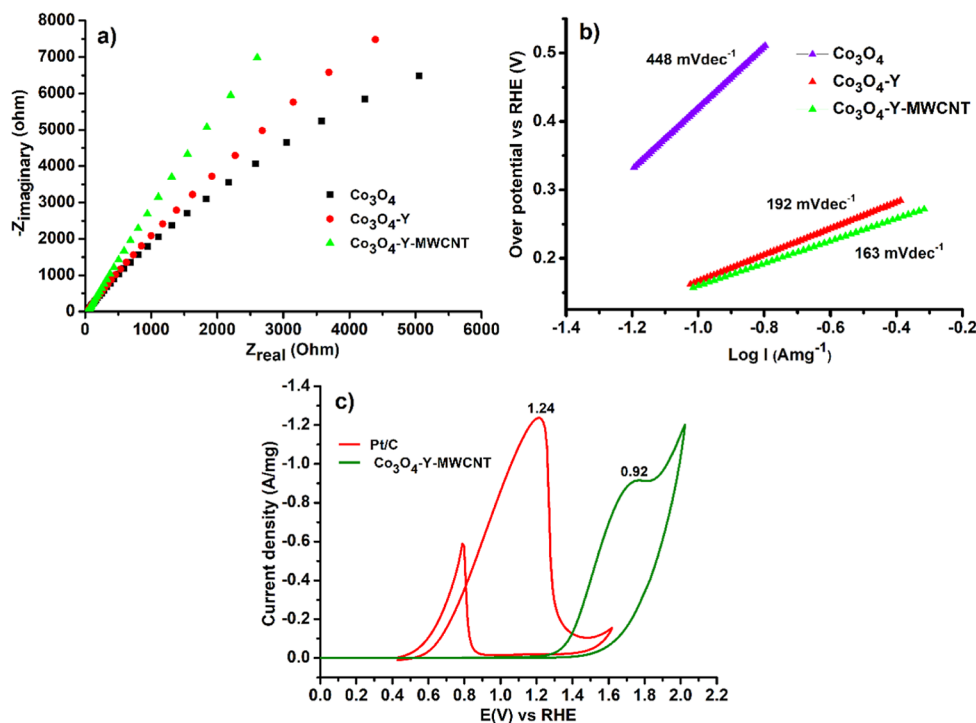

Figure 9. (a) Nyquist plot for Co$_3$O$_4$ (black), Co$_3$O$_4$-Y (red), and Co$_3$O$_4$-Y-MWCNT (green)-based electrode, (b) Tafel slope obtained from the materials Co$_3$O$_4$ (blue), Co$_3$O$_4$-Y (red), and Co$_3$O$_4$-Y-MWCNT (green) (scan rate of 50 mV s^{-1}) in 1 M KOH and 1 M CH$_3$OH, and (c) CV of 1 M CH$_3$OH with Pt/C (red line) and Co$_3$O$_4$-Y-MWCNT (green line) in 1 M KOH at a scan rate of 50 mV s^{-1}.

The electrochemical surface area (ECSA) of the materials were assessed by recording the CVs (10 to 100 mV s^{-1}) at the non-Faradaic (0−0.1 vs Ag/AgCl) potential range and calculating the electrochemical double-layer capacitance (C_{dl}) value. The plots of the ECSA measurements of Co$_3$O$_4$-Y and Co$_3$O$_4$-Y-MWCNT are depicted in Figure 8a−d. Plotting

current density versus scan rate, a straight line with a slope C_{dl} was obtained and the ECSA value was obtained by using eq 2, dividing the C_{dl} value with the specific capacitance (C_s).[8]

$$\text{ECSA} = \frac{C_{dl}}{C_s} \tag{2}$$

Scheme 2. Plausible Mechanism of Methanol Oxidation Reaction over the Catalyst Surface
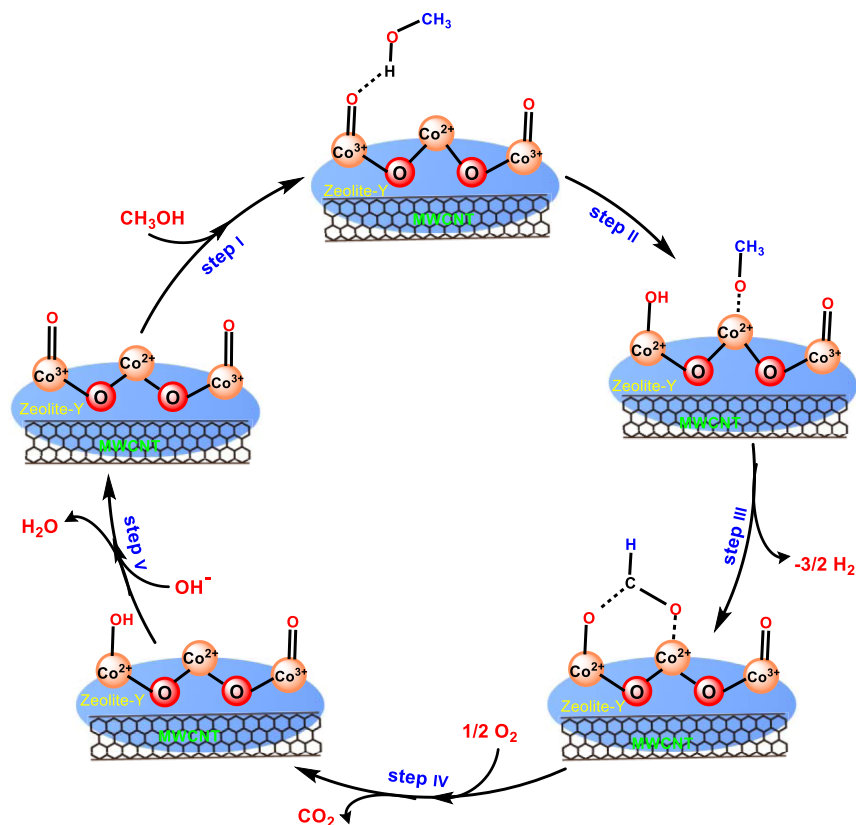
The C_{dl} value for the material Co_3O_4-Y was obtained to be 0.00047 F g^{-1} and that for the Co_3O_4-Y-MWCNT was 0.00080 F g^{-1}. The calculated C_s values were found to be 0.18×10^{-4} F g^{-1} for Co_3O_4-Y and 0.21×10^{-4} F g^{-1} for Co_3O_4-Y-MWCNT and the corresponding ECSA values were 25 and 38 m^2 g^{-1}, respectively. This also further indicated that the incorporation of the COOH-MWCNT improved the specific surface area. The electrochemical surface area provides information that the higher the ECSA value is, higher is the availability of the substrate molecule (CH$_3$OH) for the interaction. Therefore, it can be said that the incorporation of COOH-MWCNT favored the MOR process by providing a conductive surface for electron transfer and resulting in a higher specific surface area for better methanol interaction with the active catalyst species that is Co_3O_4. In addition to this, it was observed from the TGA and TPR analysis that the particle size of the active catalyst, i.e., Co_3O_4 manipulates the thermal stability. Therefore, it is expected that the particle size of Co_3O_4 also played a dominant role in enhancing the MOR activity. In this respect, zeolite-Y also played a significant role as they can control the particle size and also prevent the agglomeration and that is why probably the zeolite-Y supported catalyst along with the COOH-MWCNT resulted in good MOR activity.[20,68,70] It is pertinent to mention that in general, smaller nanoparticles have a greater surface area per unit mass in comparison to larger ones. Increased surface area helps in the electrochemical reaction providing a greater number of active sites. More surface area can result in higher catalytic activity when it comes to methanol oxidation, since it provides more active sites for methanol adsorption and oxidation. Also, the reduced nanoparticle size may speed up the reaction kinetics, thereby helping the fuel cell to operate efficiently. Many other previous reports are available which

provided the information that the particle size can manifest the electrochemical activity of nanoparticles in the MOR process.[73−75] Therefore, it is believed that a similar effect might have influenced the thermal stability as well as the MOR activity of the present catalyst, Co_3O_4-Y-MWCNT.

The electrochemical impedance spectroscopy (EIS) measurement was conducted for both the catalysts. The Nyquist plot for the catalysts Co_3O_4-Y (red) and Co_3O_4-Y-MWCNT (green) and bare Co_3O_4 (black) is shown in Figure 9a. From the plot, it was evident that the catalyst Co_3O_4-Y-MWCNT displayed an almost straight line, suggesting low charge transfer resistance in comparison to that of Co_3O_4-Y and Co_3O_4.[20] This indicated the incorporation of COOH-MWCNT to Co_3O_4-Y and this smoothed the diffusion process at the electrode interface. So, the catalyst Co_3O_4-Y-MWCNT was more efficient for MOR than Co_3O_4-Y in terms of improved current density and lower impedance diameter arc. One of the observed characteristics that correlates the activity of a catalyst is the Tafel slope. During the MOR, interaction between anode material and the CH$_3$OH takes place, resulting in the formation of some reactive intermediate as well as some poisonous species. This interaction is indicated by the Tafel plot. The Tafel plot for the materials Co_3O_4, Co_3O_4-Y, and Co_3O_4-Y-MWCNT was constructed from the CVs obtained under identical conditions in 1 M KOH and 1 M CH$_3$OH (scan rate of 50 mV s^{-1}). The slopes of the Tafel plot were calculated to be 448, 192, and 163 mV dec^{-1} for Co_3O_4 (blue), Co_3O_4-Y (red), and Co_3O_4-Y-MWCNT (green), respectively, and are depicted in Figure 9b. A lower Tafel slope value indicates a greater electrocatalytic activity of the catalyst. A lower value of the Tafel slope also suggests a higher tolerance to the poisoned species. The results attained from Tafel slope analysis revealed that among the synthesized

materials Co_3O_4, Co_3O_4-Y, and Co_3O_4-Y-MWCNT, the catalyst Co_3O_4-Y-MWCNT was found to have the lowest Tafel slope of 163 mV dec^{-1}. This indicated that the electrocatalyst Co_3O_4-Y-MWCNT possessed high tolerance to the intermediate species and was the primary cause for exhibiting higher activity in MOR compared to Co_3O_4 and Co_3O_4-Y. The exchange current densities, $j°$, for Co_3O_4, Co_3O_4-Y, and Co_3O_4-Y-MWCNT were calculated by using the Tafel equation and Tafel plot (Figure 9b) and were found to be 0.022, 0.058, and 0.063 A mg^{-1}, respectively.

The MOR activity of our best catalyst Co_3O_4-Y-MWCNT was compared with the standard Pt/C catalyst under the same electrochemical condition. The CV (at scan rate 50 mV s^{-1}) of the two catalysts are compared in Figure 9c and it depicted that the Co_3O_4-Y-MWCNT was less effective than Pt/C (current density = 1.24 A mg^{-1}, onset potential = 0.4−0.6 V vs RHE) in terms of both onset potential as well as current density which is usually expected for a single non-noble metal catalyst. However, on comparing the activity with similar other cobalt-based catalysts, the activity of our best catalyst, Co_3O_4-Y-MWCNT, was better than most of the reported ones, as provided in Table S1 of the Supporting Information. From the comparative study, it can be said that our synthesized catalyst can find a good application as the anode material in assessing the MOR activity of the non-Pt based catalyst. One of the significant outcomes of our results was that no other metal was combined with Co_3O_4, while the reported result suggested that some other metals are required to combine with Co_3O_4 to achieve a better activity in MOR. However, in our present case no such other metals were used for boosting the electrocatalyst activity of the spinel Co_3O_4. Herein, the two solid surfaces zeolite-Y and COOH-MWCNT controlled the growth of Co_3O_4 and also influenced the electronic structure through the quantum confinement effect and modulated its activity for MOR. Therefore, the present catalyst can be considered advantageous as it only used a single metal.

4.1. Plausible Mechanism of the Reaction. The mechanism of the reaction can be depicted in Scheme 2. Initially the CH_3OH will get adsorbed at the catalyst surface. After adsorption, Co_3O_4 will abstract a proton (H$^+$) from the −OH group of CH_3OH forming the methoxy ($-CH_3O^-$) species. The CH_3O^- will then be bound to the Co(II) center of the spinel Co_3O_4. During this process one of the Co(III) centers occupying the octahedral site will fluctuate its oxidation state between (II) and (III) as shown in "step II" of Scheme 2. Once the CH_3O^- ion is formed and bound to the catalyst, it will get dehydrogenated at the catalyst surface and will decompose to HCO_2^-. The HCO_2^- will interact with two cobalt centers as shown in "step III" and will further get oxidized to CO_2 and H_2O in the presence of arial oxygen (O_2), as shown in "step IV" and "step V" of Scheme 2. The OH$^-$ will be provided by the base (KOH) used during the process.

5. CONCLUSIONS

In conclusion, a non-Pt-based single metal-based electrocatalyst had been successfully synthesized via a simple and energy efficient hydrothermal process. Due to the combined impact of zeolite-Y and multiwalled carbon nanotube (COOH-MWCNT), the catalyst Co_3O_4-Y-MWCNT displayed remarkable activity toward the electrochemical oxidation of CH_3OH. The catalyst's high current density, low onset potential, high surface area, and stable current response implied that it can be used in DMFCs as an anode catalyst as a replacement to the less

stable Pt/C catalysts that are currently in use. Considering the recent increase in the market price of Pt/Pd, such a unique approach to developing nonplatinum-metal-based nanocatalysts for DMFC applications may open up new paths for utilizing zeolite-Y and COOH-MWCNT-based nanomaterials for various energy-related electrochemical applications.

■ ASSOCIATED CONTENT

ⓢ Supporting Information

The Supporting Information is available free of charge at https://pubs.acs.org/doi/10.1021/acsomega.3c06414.

> Physical measurements, DRS analysis of Co_3O_4-Y and Co_3O_4-Y-MWCNT, XPS spectra of Al and Si of Co_3O_4-Y and Co_3O_4-Y-MWCNT, XPS spectra of carbon (C) of Co_3O_4-Y-MWCNT, EDX mapping images of Co_3O_4-Y-MWCNT, CV curve in 1 M KOH of Co_3O_4-Y, CV curve in 1 M KOH of Co_3O_4-Y-MWCNT, and comparison of MOR reactivity of some cobalt-based catalysts (PDF)

■ AUTHOR INFORMATION

Corresponding Author

Kusum K. Bania − *Department of Chemical Sciences, Tezpur University, Tezpur 784028 Assam, India;* ⓞ orcid.org/0000-0001-6535-3913; Email: kusum@tezu.ernet.in, bania.kusum8@gmail.com

Authors

Salma A. Khanam − *Department of Chemical Sciences, Tezpur University, Tezpur 784028 Assam, India*

Sayanika Saikia − *Department of Chemical Sciences, Tezpur University, Tezpur 784028 Assam, India*

Seonghwan Lee − *Department of Mechanical Engineering, Ulsan National Institute of Science and Technology, Ulsan 44919, Republic of Korea*

Young-Bin Park − *Department of Mechanical Engineering, Ulsan National Institute of Science and Technology, Ulsan 44919, Republic of Korea;* ⓞ orcid.org/0000-0001-5936-7155

Magdi E. A. Zaki − *Department of Chemistry, Imam Mohammad Ibn Saud Islamic University (IMSIU), Riyadh 11623, Saudi Arabia*

Complete contact information is available at:
https://pubs.acs.org/10.1021/acsomega.3c06414

Notes

The authors declare no competing financial interest.

■ REFERENCES

(1) Chen, X.; Li, C.; Grätzel, M.; Kostecki, R.; Mao, S. S. Nanomaterials for Renewable Energy Production and Storage. *Chem. Soc. Rev.* **2012**, *41*, 7909−7937.

(2) Wang, Y.; Cao, Q.; Liu, L.; Wu, Y.; Liu, H.; Gu, Z.; Zhu, C. A Review of Low and Zero Carbon Fuel Technologies: Achieving Ship Carbon Reduction Targets. *Sustainable Energy Technol. Assess.* **2022**, *54*, 102762.

(3) Dawood, F.; Anda, M.; Shafiullah, G. M. Hydrogen Production for Energy: An Overview. *Int. J. Hydrogen Energy* **2020**, *45*, 3847−3869.

(4) Singla, M. K.; Nijhawan, P.; Oberoi, A. S. Hydrogen Fuel and Fuel Cell Technology for Cleaner Future: A Review. *Environ. Sci. Pollut. Res.* **2021**, *28*, 15607−15626.

(5) Shahjalal, M.; Shams, T.; Islam, M. E.; Alam, W.; Modak, M.; Hossain, S. B.; Ramadesigan, V.; Ahmed, M. R.; Ahmed, H.; Iqbal, A. A Review of Thermal Management for Li-Ion Batteries: Prospects, Challenges, and Issues. *J. Energy Storage* **2021**, *39*, 102518.

(6) Rodionova, M. V.; Poudyal, R. S.; Tiwari, I.; Voloshin, R. A.; Zharmukhamedov, S. K.; Nam, H. G.; Zayadan, B. K.; Bruce, B. D.; Hou, H. J.; Allakhverdiev, S. I. Biofuel Production: Challenges and Opportunities. *Int. J. Hydrogen Energy* **2017**, *42*, 8450−8461.

(7) Cousins, K.; Zhang, R. Highly Porous Organic Polymers for Hydrogen Fuel Storage. *Polymers* **2019**, *11*, 690.

(8) Wang, Y.; Suzuki, H. L.; Xie, J.; Tomita, O.; Martin, D. J.; Higashi, M.; Kong, D.; Abe, R.; Tang, J. Mimicking Natural Photosynthesis: Solar to Renewable H_2 Fuel Synthesis by Z-Scheme Water Splitting Systems. *Chem. Rev.* **2018**, *118*, 5201−5241.

(9) Verhelst, S.; Turner, J. W.; Sileghem, L.; Vancoillie, J. Methanol as A Fuel for Internal Combustion Engines. *Prog. Energy Combust. Sci.* **2019**, *70*, 43−88.

(10) Simon Araya, S.; Liso, V.; Cui, X.; Li, N.; Zhu, J.; Sahlin, S. L.; Jensen, S. H.; Nielsen, M. P.; Kær, S. K. A Review of the Methanol Economy: The Fuel Cell Route. *Energies* **2020**, *13*, 596.

(11) Hankin, A.; Shah, N. Process Exploration and Assessment for the Production of Methanol and Dimethyl Ether from Carbon Dioxide and Water. *Sustainable Energy Fuels* **2017**, *1*, 1541−1556.

(12) Al-Rowaili, F. N.; Jamal, A.; Ba Shammakh, M. S.; Rana, A. A Review on Recent Advances for Electrochemical Reduction of Carbon Dioxide to Methanol Using Metal-Organic Framework (MOF) and Non-MOF Catalysts: Challenges and Future Prospects. *ACS Sustainable Chem. Eng.* **2018**, *6*, 15895−15914.

(13) Alias, M. S.; Kamarudin, S. K.; Zainoodin, A. M.; Masdar, M. S. Active Direct Methanol Fuel Cell: An Overview. *Int. J. Hydrogen Energy* **2020**, *45*, 19620−19641.

(14) Kumar, P.; Dutta, K.; Das, S.; Kundu, P. P. An Overview of Unsolved Deficiencies of Direct Methanol Fuel Cell Technology: Factors and Parameters Affecting its Widespread Use. *Int. J. Energy Res.* **2014**, *38*, 1367−1390.

(15) Wang, X.; Xi, S.; Lee, W. S. V.; Huang, P.; Cui, P.; Zhao, L.; Hao, W.; Zhao, X.; Wang, Z.; Wu, H.; et al. Materializing Efficient Methanol Oxidation via Electron Delocalization in Nickel Hydroxide Nano-ribbon. *Nat. Commun.* **2020**, *11*, 4647.

(16) Karlberg, G. S.; Rossmeisl, J.; Nørskov, J. K. Estimations of Electric Field Effects on the Oxygen Reduction Reaction Based on the Density Functional Theory. *Phys. Chem. Chem. Phys.* **2007**, *9*, 5158−5161.

(17) Léger, J. M. Mechanistic Aspects of Methanol Oxidation on Platinum-Based Electrocatalysts. *J. Appl. Electrochem.* **2001**, *31*, 767−771.

(18) Tian, H.; Yu, Y.; Wang, Q.; Li, J.; Rao, P.; Li, R.; Du, Y.; Jia, C.; Luo, J.; Deng, P.; Shen, Y.; et al. Recent Advances in Two-Dimensional Pt Based Electrocatalysts for Methanol Oxidation Reaction. *Int. J. Hydrogen Energy* **2021**, *46*, 31202−31215.

(19) Khanam, S. A.; Hoque, N.; Lee, S.; Park, Y. B.; Gogoi, G.; Bania, K. K. Tubular Nickel Hydroxide Embedded in Zeolitic Cobalt Oxide for Methanol Oxidation Reaction. *ACS Appl. Energy Mater.* **2022**, *5*, 12651−12662.

(20) Hoque, N.; Baruah, M. J.; Lee, S.; Park, Y. B.; Dutta, R.; Roy, S.; Bania, K. K. Cu(OH)₂-Ni(OH)₂ Engulfed by Zeolite-Y Hydroxyl Nest and Multiwalled Carbon Nanotube for Effective Methanol Oxidation Reaction. *Electrochim. Acta* **2021**, *397*, 139313.

(21) Hoque, N.; Lee, S.; Park, Y. B.; Roy, S.; Baruah, M. J.; Biswas, S.; Gogoi, G.; Bora, T. J.; Dutta, R.; Bania, K. K. Dual Matrix Influence on Ni (II) Rich Hybrid Catalyst for Electrochemical Methanol Oxidation Reaction. *ChemNanoMat* **2022**, *8*, 202200280.

(22) Fu, X.; Wan, C.; Huang, Y.; Duan, X. Noble Metal Based Electrocatalysts for Alcohol Oxidation Reactions in Alkaline Media. *Adv. Funct. Mater.* **2022**, *32*, 2106401.

(23) Spendelow, J. S.; Wieckowski, A. Electrocatalysis of Oxygen Reduction and Small Alcohol Oxidation in Alkaline Media. *Phys. Chem. Chem. Phys.* **2007**, *9*, 2654−2675.

(24) Antolini, E.; Gonzalez, E. R. Alkaline Direct Alcohol Fuel Cells. *J. Power Sources* **2010**, *195*, 3431−3450.

(25) Feng, Y. Y.; Bi, L. X.; Liu, Z. H.; Kong, D. S.; Yu, Z. Y. Significantly Enhanced Electrocatalytic Activity for Methanol Electro-Oxidation on Ag Oxide-Promoted PtAg/C Catalysts in Alkaline Electrolyte. *J. Catal.* **2012**, *290*, 18−25.

(26) Sharma, M.; Das, B.; Baruah, M. J.; Biswas, S.; Roy, S.; Hazarika, A.; Bhargava, S. K.; Bania, K. K. Pd-Au-Y as Efficient Catalyst for C-C Coupling Reactions, Benzylic C-H Bond Activation, and Oxidation of Ethanol for Synthesis of Cinnamaldehydes. *ACS Catal.* **2019**, *9*, 5860−5875.

(27) Sharma, M.; Das, B.; Sharma, M.; Deka, B. K.; Park, Y. B.; Bhargava, S. K.; Bania, K. K. Pd/Cu-Oxide Nanoconjugate at Zeolite-Y Crystallite Crafting the Mesoporous Channels for Selective Oxidation of Benzyl-Alcohols. *ACS Appl. Mater. Interfaces* **2017**, *9*, 35453−35462.

(28) Sharma, M.; Das, B.; Hazarika, A.; Guha, A. K.; Bhargava, S. K.; Bania, K. K. PdO/CuO Nanoparticles on Zeolite-Y for Nitroarene Reduction and Methanol Oxidation. *ACS Appl. Mater. Interfaces* **2019**, *2*, 3769−3779.

(29) Samanta, S.; Bhunia, K.; Pradhan, D.; Satpati, B.; Srivastava, R. NiCuCo₂O₄ Supported Ni-Cu Ion-Exchanged Mesoporous Zeolite Heteronano Architecture: An Efficient, Stable, and Economical Nonprecious Electrocatalyst for Methanol Oxidation. *ACS Sustainable Chem. Eng.* **2018**, *6*, 2023−2036.

(30) Medina Ramirez, A.; Ruiz Camacho, B.; Villicaña Aguilera, M.; Galindo Esquivel, I.; Ramírez-Minguela, J. Effect of Different Zeolite as Pt Supports for Methanol Oxidation Reaction. *Appl. Surf. Sci.* **2018**, *456*, 204−214.

(31) Mohan, N.; Cindrella, L. Template-free Synthesis of Pt-MOx (M= Ni, Co & Ce) Supported on Cubic Zeolite-A and their Catalytic Role in Methanol Oxidation and Oxygen Reduction Reactions Characterized by the Hydrodynamic Study. *Int. J. Hydrogen Energy* **2017**, *42*, 21719−21731.

(32) Li, J.; Luo, Z.; He, F.; Zuo, Y.; Zhang, C.; Liu, J.; Yu, X.; Du, R.; Zhang, T.; Infante-Carrio, M. F.; Tang, P.; et al. Colloidal Ni-Co-Sn Nanoparticles as Efficient Electrocatalysts for the Methanol Oxidation Reaction. *J. Mater. Chem. A* **2018**, *6*, 22915−22924.

(33) Askari, M. B.; Rozati, S. M. Construction of Co₃O₄-Ni₃S₄-rGO Ternary Hybrid as An Efficient Nanoelectrocatalyst for Methanol and Ethanol Oxidation in Alkaline Media. *J. Alloys Compd.* **2022**, *900*, 163408.

(34) Cao, Y.; Ge, J.; Jiang, M.; Zhang, F.; Lei, X. Acid-Etched Co₃O₄ Nanoparticles on Nickel Foam: The Highly Reactive (311) Facet and Enriched Defects for Boosting Methanol Oxidation Electrocatalysis. *ACS Appl. Mater. Interfaces* **2021**, *13*, 29491−29499.

(35) Wang, C.; Luo, J.; Dou, H.; Raise, A.; Ali, M. S.; Fan, W.; Li, Q. Optimization and Analytical Behavior of A Morphine Electrochemical Sensor in Environmental and Biological Samples Based on Graphite Rod Electrode Using Graphene/Co₃O₄ Nanocomposite. *Chemosphere* **2023**, *326*, 138451.

(36) Wang, H.; Li, S.; Sun, G.; Lu, G.; Bu, Q.; Kong, X.; Liu, Q. Trace W-Doping Flocculent Co₃O₄ Nanostructures with Enhanced Electrocatalytic Performance for Methanol Oxidation Reaction. *Inorg. Chem. Commun.* **2022**, *145*, 109984.

(37) Zhang, G.; Li, J. H. Tailoring Oxygen Vacancy on Co₃O₄ Nanosheets with High Surface Area for Oxygen Evolution Reaction. *Chin. J. Chem. Phys.* **2018**, *31*, 517−522.

(38) Deng, X.; Tüysüz, H. Cobalt-Oxide-Based Materials as Water Oxidation Catalyst: Recent Progress and Challenges. *ACS Catal.* **2014**, *4*, 3701−3714.

(39) Goel, J.; Basu, S. Effect of Support Materials on the Performance of Direct Ethanol Fuel Cell Anode Catalyst. *Int. J. Hydrogen Energy* **2014**, *39*, 15956−15966.

(40) Ward, J. W. Spectroscopic Study of the Surface of Zeolite Y. II. Infrared Spectra of Structural Hydroxyl Groups and Adsorbed Water on Alkali, Alkaline Earth, and Rare Earth Ion-Exchanged Zeolites. *J. Phys. Chem.* **1968**, *72*, 4211−4223.

(41) He, T.; Chen, D.; Jiao, X. Controlled Synthesis of Co_3O_4 Nanoparticles through Oriented Aggregation. *Chem. Mater.* **2004**, *16*, 737−743.

(42) Li, Y.; Qiu, W.; Qin, F.; Fang, H.; Hadjiev, V. G.; Litvinov, D.; Bao, J. Identification of Cobalt Oxides with Raman Scattering and Fourier Transform Infrared Spectroscopy. *J. Phys. Chem. C* **2016**, *120*, 4511−4516.

(43) De Menezes, B. R. C.; Ferreira, F. V.; Silva, B. C.; Simonetti, E. A. N.; Bastos, T. M.; Cividanes, L. S.; Thim, G. P. Effects of Octadecylamine Functionalization of Carbon Nanotubes on Dispersion, Polarity, and Mechanical Properties of CNT/HDPE Nanocomposites. *J. Mater. Sci.* **2018**, *53*, 14311−14327.

(44) Ando, Y.; Zhao, X.; Shimoyama, H.; Sakai, G.; Kaneto, K. Physical Properties of Multiwalled Carbon Nanotubes. *Int. J. Inorg. Mater.* **1999**, *1*, 77−82.

(45) Ren, Q.; Feng, Z.; Mo, S.; Huang, C.; Li, S.; Zhang, W.; Chen, L.; Fu, M.; Wu, J.; Ye, D. 1D-Co_3O_4, 2D-Co_3O_4, 3D-Co_3O_4 for Catalytic Oxidation of Toluene. *Catal. Today* **2019**, *332*, 160−167.

(46) Davar, F.; Fereshteh, Z.; Shoja Razavi, H.; Razavi, R. S.; Loghman-Estarki, M. R. Synthesis and Characterization of Cobalt Oxide Nanocomposite based on the Co_3O_4-Zeolite Y. *Superlattices Microstruct.* **2014**, *66*, 85−95.

(47) Chuang, T. J.; Brundle, C. R.; Rice, D. W. Interpretation of the X-Ray Photoemission Spectra of Cobalt Oxides and Cobalt Oxide Surfaces. *Surf. Sci.* **1976**, *59*, 413−429.

(48) Hadjiev, V. G.; Iliev, M. N.; Vergilov, I. V. The Raman Spectra of Co_3O_4. *J. Phys. C: Solid State Phys.* **1988**, *21*, L199−L201.

(49) Zhang, S.; Huang, J.; Yu, Y.; Wang, S.; Yang, T.; Zhang, Z.; Tong, L.; Zhang, J. Quantum Interference Directed Chiral Raman Scattering in Two-Dimensional Enantiomers. *Nat. Commun.* **2022**, *13*, 1254.

(50) Miranda, H. P.; Reichardt, S.; Froehlicher, G.; Molina-Sánchez, A.; Berciaud, S.; Wirtz, L. Quantum Interference Effects in Resonant Raman Spectroscopy of Single-and Triple-Layer $MoTe_2$ from First-Principles. *Nano Lett.* **2017**, *17*, 2381−2388.

(51) Osiekowicz, M.; Staszczuk, D.; Olkowska-Pucko, K.; Kipczak, Ł.; Grzeszczyk, M.; Zinkiewicz, M.; Nogajewski, K.; Kudrynskyi, Z. R.; Kovalyuk, Z. D.; Patané, A.; Babiński, A.; et al. Resonance and Antiresonance in Raman Scattering in GaSe and InSe Crystals. *Sci. Rep.* **2021**, *11*, 924.

(52) Chen, C. F.; Park, C. H.; Boudouris, B. W.; Horng, J.; Geng, B.; Girit, C.; Zettl, A.; Crommie, M. F.; Segalman, R. A.; Louie, S. G.; Wang, F. Controlling Inelastic Light Scattering Quantum Pathways in Graphene. *Nature* **2011**, *471*, 617−620.

(53) Zdrojek, M.; Gebicki, W.; Jastrzebski, C.; Melin, T.; Huczko, A. Studies of Multiwall Carbon Nanotubes Using Raman Spectroscopy and Atomic Force Microscopy. *Solid State Phenom.* **2004**, *99−100*, 265−268.

(54) Sathyaseelan, A.; Elumalai, V.; Krishnamoorthy, K.; Sajeev, A.; Kim, S. J. Sphere-like PdNi Alloy: Unveiling the Twin Functional Properties toward Oxygen Reduction and Temperature-Dependent Methanol Oxidation for Alkaline Direct Methanol Fuel Cells. *ACS Sustain. Chem. Eng.* **2023**, *11*, 5345−5355.

(55) Meher, S. K.; Rao, G. R. Polymer-Assisted Hydrothermal Synthesis of Highly Reducible Shuttle-Shaped CeO_2: Microstructural Effect on Promoting Pt/C for Methanol Electrooxidation. *ACS Catal.* **2012**, *2*, 2795−2809.

(56) Mahdavi, H.; Panahi, M. K. S.; Shahalizade, T. Preparation and Application of Hyperbranched Polymer-Modified Polyethersulfone Membrane Containing Ni-Pd-Sn-Coated MWCNT for Catalytic Aryl Halide Coupling Reactions. *Polym. Bull.* **2018**, *75*, 5677−5694.

(57) Yıldırım, A.; Seçkin, T. In Situ Preparation of Polyether Amine Functionalized MWCNT Nanofiller as Reinforcing Agents. *Adv. Mater. Sci. Eng.* **2014**, *2014*, 356920.

(58) Tao, Y.; Kanoh, H.; Kaneko, K. Uniform Mesopore-Donated Zeolite Y Using Carbon Aerogel Templating. *J. Phys. Chem. B* **2003**, *107*, 10974−10976.

(59) Kumar, N.; Yu, Y. C.; Lu, Y. H.; Tseng, T. Y. Fabrication of Carbon Nanotube/Cobalt Oxide Nanocomposites via Electrophoretic Deposition for Supercapacitor Electrodes. *J. Mater. Sci.* **2016**, *51*, 2320−2329.

(60) Singh, B. P.; Singh, D.; Mathur, R. B.; Dhami, T. L. Influence of Surface Modified MWCNTs on the Mechanical, Electrical and Thermal Properties of Polyimide Nanocomposites. *Nanoscale Res. Lett.* **2008**, *3*, 444.

(61) Wang, Y.; Wei, X.; Hu, X.; Zhou, W.; Zhao, Y. Effect of Formic Acid Treatment on the Structure and Catalytic Activity of Co_3O_4 for N_2O Decomposition. *Catal. Lett.* **2019**, *149*, 1026−1036.

(62) James, O. O.; Maity, S. Temperature Programme Reduction (TPR) Studies of Cobalt Phases In-Alumina Supported Cobalt Catalysts. *J. Pet. Technol. Altern. Fuels* **2016**, *7*, 1−12.

(63) Li, J.; Xu, X.; Hao, Z.; Zhao, W. Mesoporous Silica Supported Cobalt Oxide Catalysts for Catalytic Removal of Benzene. *J. Porous Mater.* **2008**, *15*, 163−169.

(64) Mahammadunnisa, S. K.; Akanksha, T.; Krushnamurty, K.; Subrahmanyam, C. H. Catalytic Decomposition of N_2O over CeO_2 Supported Co_3O_4 Catalysts. *J. Chem. Sci.* **2016**, *128*, 1795−1804.

(65) Ambika, S.; Gopinath, S.; Saravanan, K.; Sivakumar, K.; Ragupathi, C.; Sukantha, T. A. Structural, Morphological and Optical Properties and Solar Cell Applications of Thioglycolic Routed Nano Cobalt Oxide Material. *Energy Rep.* **2019**, *5*, 305−309.

(66) Barreca, D.; Massignan, C.; Daolio, S.; Fabrizio, M.; Piccirillo, C.; Armelao, L.; Tondello, E. Composition and Microstructure of Cobalt Oxide Thin Films Obtained from a Novel Cobalt (II) Precursor by Chemical Vapor Deposition. *Chem. Mater.* **2001**, *13*, 588−593.

(67) Amoo, C. C.; Li, M.; Noreen, A.; Fu, Y.; Maturura, E.; Du, C.; Yang, R.; Gao, X.; Xing, C.; Tsubaki, N. Fabricating Fe Nanoparticles Embedded in Zeolite Y Microcrystals as Active Catalysts for Fischer−Tropsch Synthesis. *ACS Appl. Nano Mater.* **2020**, *3*, 8096−8103.

(68) Hoque, N.; Baruah, M. J.; Biman, A. H.; Biswas, S.; Gogoi, G.; Dutta, R.; Bania, K. K. Impregnating Rhodium (0) Sites Through Zeolite-Y Templation in A Hybrid Rh-Ni Catalyst for Alcohol Electro-Oxidation with Low CO Poisoning. *ACS Appl. Energy Mater.* **2022**, *5*, 6118−6128.

(69) Kim, N.; Park, H.; Yoon, N.; Lee, J. K. Zeolite-Templated Mesoporous Silicon Particles for Advanced Lithium-Ion Battery Anodes. *ACS Nano* **2018**, *12*, 3853−3864.

(70) Sharma, M.; Das, B.; Baruah, M. J.; Bhattacharyya, P. K.; Saikia, L.; Bania, K. K. Pd-NiO-Y/CNT Nanofoam: A Zeolite-Carbon Nanotube Conjugate Exhibiting High Durability in Methanol Oxidation. *Chem. Commun.* **2020**, *56*, 375−378.

(71) Lee, J. S.; Jo, M. S.; Saroha, R.; Jung, D. S.; Seon, Y. H.; Lee, J. S.; Kang, Y. C.; Kang, D. W.; Cho, J. S. Hierarchically Well-Developed Porous Graphene Nanofibers Comprising N-Doped Graphitic C-Coated Cobalt Oxide Hollow Nanospheres as Anodes for High-Rate Li-Ion Batteries. *Small* **2020**, *16*, 2002213.

(72) Wang, X.; Xi, S.; Lee, W. S. V.; Huang, P.; Cui, P.; Zhao, L.; Hao, W.; Zhao, X.; Wang, Z.; Wu, H.; Wang, H.; et al. Materializing Efficient Methanol Oxidation Via Electron Delocalization in Nickel Hydroxide Nanoribbon. *Nat. Commun.* **2020**, *11*, 4647.

(73) Bergamaski, K.; Pinheiro, A. L.; Teixeira-Neto, E.; Nart, F. C. Nanoparticle Size Effects on Methanol Electrochemical Oxidation on Carbon Supported Platinum Catalysts. *J. Phys. Chem. B* **2006**, *110*, 19271−19279.

(74) Rhee, C. K.; Kim, B. J.; Ham, C.; Kim, Y. J.; Song, K.; Kwon, K. Size Effect of Pt Nanoparticle on Catalytic Activity in Oxidation of Methanol and Formic Acid: Comparison to Pt (111), Pt (100), and Polycrystalline Pt Electrodes. *Langmuir* **2009**, *25*, 7140−7147.

(75) Park, S.; Xie, Y.; Weaver, M. J. Electrocatalytic Pathways on Carbon-Supported Platinum Nanoparticles: Comparison of Particle-Size-Dependent Rates of Methanol, Formic Acid, and Formaldehyde Electrooxidation. *Langmuir* **2002**, *18*, 5792−5798.